

DISK–STELLAR MUTUAL INCLINATIONS AND RECURRENT ECLIPSES IN THE YOUNG AND MASSIVE GW ORI TRIPLE SYSTEM

IAN CZEKALA,^{1,*} SEAN M. ANDREWS,² GUILLERMO TORRES,² JOSEPH E. RODRIGUEZ,² ERIC L. N. JENSEN,³
KEIVAN G. STASSUN,^{4,5} DAVID W. LATHAM,² DAVID J. WILNER,² MICHAEL A. GULLY-SANTIAGO,⁶ MICHAEL B. LUND,⁷
RUDOLF B. KUHN,⁸ DANIEL J. STEVENS,⁹ ROBERT J. SIVERD,¹⁰ DAVID JAMES,¹¹ B. SCOTT GAUDI,⁹
KONSTANTIN N. GRANKIN,¹² BENJAMIN J. SHAPPEE,^{13,†} KRZYSZTOF Z. STANEK,^{9,14} THOMAS W.-S. HOLOIEN,^{9,14,15}
CHRISTOPHER S. KOCHANEK,^{9,14} AND JOSE L. PRIETO^{16,17}

¹*Kavli Institute for Particle Astrophysics and Cosmology, Stanford University, 452 Lomita Mall, Stanford, CA 94305, USA*

²*Harvard-Smithsonian Center for Astrophysics, 60 Garden Street, Cambridge, MA 02138, USA*

³*Department of Physics and Astronomy, Swarthmore College, 500 College Avenue, Swarthmore, PA 19081, USA*

⁴*Department of Physics and Astronomy, Vanderbilt University, Nashville, TN 37235, USA*

⁵*Department of Physics, Fisk University, Nashville, TN 37208, USA*

⁶*NASA Ames*

⁷*Department of Physics and Astronomy, Vanderbilt University, 6301 Stevenson Center, Nashville, TN 37235, USA*

⁸*South African Astronomical Observatory, P.O. Box 9, Observatory 7935, South Africa*

⁹*Department of Astronomy, The Ohio State University, Columbus, OH 43210, USA*

¹⁰*Las Cumbres Observatory Global Telescope Network, 6740 Cortona Drive, Suite 102, Santa Barbara, CA 93117, USA*

¹¹*Astronomy Department, University of Washington, Box 351580, Seattle, WA 98195, USA*

¹²*Crimean Astrophysical Observatory, pos. Nauchnyi, Crimea, 298409 Russia*

¹³*Carnegie Observatories, 813 Santa Barbara Street, Pasadena, CA 91101, USA*

¹⁴*Center for Cosmology and Astroparticle Physics, The Ohio State University, 191 W. Woodruff Ave., Columbus, OH 43210, USA*

¹⁵*US Department of Energy Computational Science Graduate Fellow*

¹⁶*Nucleo de Astronomia de la Facultad de Ingeniera, Universidad Diego Portales, Av. Ejercito 441, Santiago, Chile*

¹⁷*Millennium Institute of Astrophysics, Santiago, Chile*

ABSTRACT

We present spatially and spectrally resolved Atacama Large Millimeter/submillimeter Array (ALMA) observations of gas and dust in the large disk orbiting the pre-main sequence hierarchical triple star system GW Ori. We forward-model the ^{13}CO and C^{18}O $J=2-1$ transitions to precisely constrain the total stellar mass to be $5.29 \pm 0.09 M_{\odot}$, and the circumtriple disk inclination to be $i_{\text{disk}} = 137.6 \pm 2.0^\circ$. We use 35 years of optical spectra to derive new radial velocity (RV) solutions and apply spectroscopic disentangling techniques to reveal that the A and B components of GW Ori form a double-lined spectroscopic binary ($P_{\text{in}} = \textcolor{red}{XX}$ days) with an outer hierarchical triple with $P_{\text{out}} = \textcolor{red}{XX}$ days. Combining the disk and RV measurements with three epochs of archival astrometry yields precise constraints on the individual stellar masses ($M_A = \textcolor{red}{XX} M_{\odot}$, $M_B = \textcolor{red}{XX} M_{\odot}$, $M_C = \textcolor{red}{XX} M_{\odot}$) and strongly indicates that at least one and possibly both stellar orbits are misaligned with the disk by as much as 45° . We also compile a 30-year V -band light curve, which reveals several ~ 20 day eclipse events 0.25 - 0.50 mag in depth. We show a tentative correlation between the times of the eclipses and the phase of the outer orbit, which suggests that the eclipses are due to the dynamical influence of the misaligned stellar orbits on the circumtriple disk. Lastly, we conclude that our measurements of stellar masses and photospheric properties are consistent with the predictions of leading pre-main sequence evolutionary models, and indicate that the GW Ori system is $\textcolor{red}{XX}$ Myr old.

Keywords: protoplanetary disks – stars: fundamental parameters – stars: pre-main sequence – stars: individual (GW Ori)

1. INTRODUCTION

Pre-main sequence stars in multiple systems—for which it is possible to precisely measure their fundamental stellar properties through dynamical means—serve as touchstones for understanding the final stages of stellar formation and the conditions under which planetary systems are assembled. While recent decades have seen steady progress in understanding binary formation in general, lingering uncertainties still remain about the characteristics of young close-in spectroscopic binaries and higher order systems (Duchêne & Kraus 2013). GW Ori, a member of the λ Orionis OB star forming complex (Dolan 2000; Dolan & Mathieu 2001, 2002), was one of the first T Tauri stars to be revealed as a spectroscopic binary, with a composite G spectral type and an orbital period of 240 days (Mathieu et al. 1991). Long term radial velocity monitoring hinted at the presence of a third body in the system with a period of \sim 10 years and was subsequently confirmed by infrared interferometry (Berger et al. 2011). The most recent and precise measurements of the distance to Orion Nebula Complex is a VLBA parallax measurement of 388 ± 5 pc (Kounkel et al. 2017), which we adopt as the distance to GW Ori.

A reservoir of circumstellar material orbiting GW Ori was inferred from near and far-infrared emission in excess of the stellar photosphere (Mathieu et al. 1991), and was subsequently confirmed by a strong single-dish detection of the dust continuum at sub-millimeter wavelengths, suggesting the presence of a massive circumstellar disk ($M_{\text{disk}} \gtrsim 0.1 M_{\odot}$; Mathieu et al. 1995). This detection provided a natural explanation for the quasi-periodic photometric dimminings of GW Ori, which were observed to occur on \sim 30 day timescales and were suspected to be due from material in the circumstellar disk occulting the primary star at edge-on inclinations ($i_{\text{disk}} \approx 90^\circ$; Shevchenko et al. 1992, 1998). Fang et al. (2017) spatially resolved the disk with Submillimeter Array (SMA) observations of the dust continuum and CO isotopologues, and revealed it to be massive ($M_{\text{disk}} = 0.12 M_{\odot}$) and large, with the CO gas significantly more extended ($r_{\text{gas}} \sim 1300$ au) than the dust ($r_{\text{dust}} \sim 400$ au), and clearly encircling all three stars.

However, they found the circumtriple disk to be at an *intermediate* inclination to the line of sight ($i_{\text{disk}} \approx 35^\circ$), challenging the assumption that the eclipses are due to material in an edge-on disk and instead suggesting that more complex dynamics are at play in the innermost radii of the system. Indeed, this adds to the collection of other indirect evidence pointing to a complicated geometry in the inner disk: a spectral energy distribution (SEDs) whose mid-infrared fluxes are variable on the timescale of years (Fang et al. 2014), and mid-infrared spectroscopic detections of CO fundamental emission with line profiles that have both a narrow and broad component, requiring a complicated emission region and temperature structure in the inner disk (Najita et al. 2003).

Beyond resolving outstanding questions about its architecture, given its large nominal primary mass but late composite spectral type ($M_{\text{A}} = 3.9 M_{\odot}$, SpT = G8; Fang et al. 2014, 2017), the GW Ori system presents an excellent opportunity to obtain a precise dynamical mass measurement of a high mass star at a very young age. Precise dynamical masses, especially on the pre-Main Sequence, are crucial to calibrating the photospheric predictions (e.g., T_{eff} , L) of stellar evolutionary models, and the region of the Hertzsprung-Russell diagram (HRD) occupied by GW Ori A is particularly sparsely populated with benchmark systems. GW Ori presents an excellent target for benchmarking because three independent dynamical mass techniques can be brought to bear on it simultaneously: radial velocity monitoring, which constrain the mass ratios of the stars (Mathieu et al. 1991; Fang et al. 2014); astrometric monitoring, which provides the inclinations of the orbits and when coupled with radial velocity measurements can reveal the individual masses of the stars (Berger et al. 2011); and the disk-based dynamical mass technique (e.g., Rosenfeld et al. 2012; Czekala et al. 2015, 2016), which directly measures the total stellar mass but unlike the first two techniques does not require long-term monitoring, instead the results can be obtained with a single resolved sub-mm observation—an important consideration given the long orbital periods involved.

In this paper, we report resolved sub-mm observations of the GW Ori system with the ALMA interferometer, which confirm the results of Fang et al. (2017) in finding a large and massive protoplanetary disk. We

* KIPAC Postdoctoral Fellow

† Hubble, Carnegie-Princeton Fellow

forward-model the ALMA observations to precisely infer the total mass of the enclosed stars and the disk inclination. We re-analyze 35 years of optical spectra to reveal GW Ori as a low semi-amplitude spectroscopic binary, and derive updated orbital constraints on GW Ori A, B, and C to conclude that the A-B orbit and possibly the AB - C orbit are strongly misaligned with the circum-triple disk. Adding in three epochs of astrometry from Berger et al. (2011) in a joint fit reinforces these conclusions. We evaluate our mass measurements of the stars in context with their photospheric properties to determine their agreement with leading pre-main sequence models. We also present an updated light curve with a 30-year baseline, which shows several new eclipse events. We conclude by discussing the structure and orientation of the protoplanetary disk with respect to the putative orbital inclinations of the stellar components and place the quasi-period eclipsing nature of GW Ori in the context of other recently discovered “dipper” stars (e.g., Ansdel et al. 2016a,b).

2. OBSERVATIONS AND DATA REDUCTION

2.1. Millimeter Interferometry

GW Ori was observed with the ALMA interferometer on 2015 May 14 (program ID 2012.1.00496.S), with 37 of the 12 m main array antennas configured to span baselines of 23–558 m. The double sideband Band 6 receivers were employed in dual polarization mode, and the ALMA correlator was set up to process data in 4 spectral windows (SPWs). Two of these SPWs, centered at 220.426 and 230.450 GHz to observe the nearby ^{13}CO and ^{12}CO $J=2-1$ transitions (at rest frequencies of 220.399 and 230.538 GHz, respectively), covered 234 MHz of bandwidth in 3840 channels (a 61 kHz channel spacing). One other sampled 469 MHz around 219.763 GHz to observe the nearby C^{18}O $J=2-1$ transition (at rest frequency 219.560 GHz) with 3840 channels (a 122 kHz channel spacing). The last SPW sampled the continuum in a 1.875 GHz range around 231.956 GHz using 128 coarse channels (a 15.625 MHz channel spacing).

The observations cycled between GW Ori and the quasar J0510+1800 with a 7 minute cadence. The quasar J0423-0120 and Ganymede were observed as bandpass and flux calibration sources, respectively, at the start of the execution block. The total on-source integration time for GW Ori was 16 minutes. The observing conditions were typical for Band 6 projects, with a precipitable water vapor level around 1.1 mm.

The visibility data were calibrated with standard procedures using the CASA software package (v4.4). The raw, observed visibility phases were adjusted based on the contemporaneous measurements of water vapor ra-

dimeters, flagged when applicable, and then the bandpass shape in (and between) each SPW was calibrated based on the observations of J0423-0120. The absolute amplitude scale was determined based on the observations of Ganymede. The complex gain behavior of the array and atmosphere was corrected based on the repeated observations of J0510+1800. The calibrated visibilities showed a strong continuum signal, suggesting that self-calibration could significantly improve the data quality. An initial model based on a preliminary continuum image was used for two rounds of phase-only self-calibration (on 30 s, then 6 s intervals) and one additional round that included the amplitudes (on a 7 minute scan interval). This self-calibration reduced the RMS noise level in the continuum by a factor of ~ 40 . After applying the self-calibration tables to the entire dataset (channel by channel), we parsed out data products for each individual emission tracer of interest. A set of continuum visibilities was constructed by spectrally averaging the line-free channels in each SPW into ~ 125 MHz increments. The spectral visibilities for the ^{12}CO , ^{13}CO , and C^{18}O lines were continuum-subtracted and regridded into 170 m s^{-1} -wide channels in the LSRK restframe over a $\sim 10 \text{ km s}^{-1}$ range around the line centers.

These fully reduced visibility sets were then imaged by Fourier inversion assuming a Briggs (robust=0.5) weighting scheme and deconvolution with the standard CLEAN algorithm. Some basic image properties for the synthesized continuum image and spectral line image cubes are listed in Table 1. The continuum and spectral line moment maps are shown together in Figure 1, along with a comparison of the integrated spectra. The channel maps for individual lines are compiled in Figure 2.

The 226 GHz (1.3 mm) continuum map shows a bright (flux density = 202 mJy), compact but marginally resolved (deconvolved Gaussian FWHM $\approx 0.^{\prime\prime}9$) source

Table 1. ALMA Image Properties

	RMS	
	beam dimensions	mJy beam^{-1}
226 GHz continuum	$0.^{\prime\prime}.88 \times 0.^{\prime\prime}.54, 126^{\circ}$	0.055
$^{12}\text{CO } J=2-1$	$0.^{\prime\prime}.89 \times 0.^{\prime\prime}.56, 126^{\circ}$	6
$^{13}\text{CO } J=2-1$	$0.^{\prime\prime}.93 \times 0.^{\prime\prime}.59, 126^{\circ}$	8
$\text{C}^{18}\text{O } J=2-1$	$0.^{\prime\prime}.92 \times 0.^{\prime\prime}.58, 126^{\circ}$	5

NOTE—The RMS noise levels recorded for the spectral line cubes correspond to the values per 170 m s^{-1} channel.

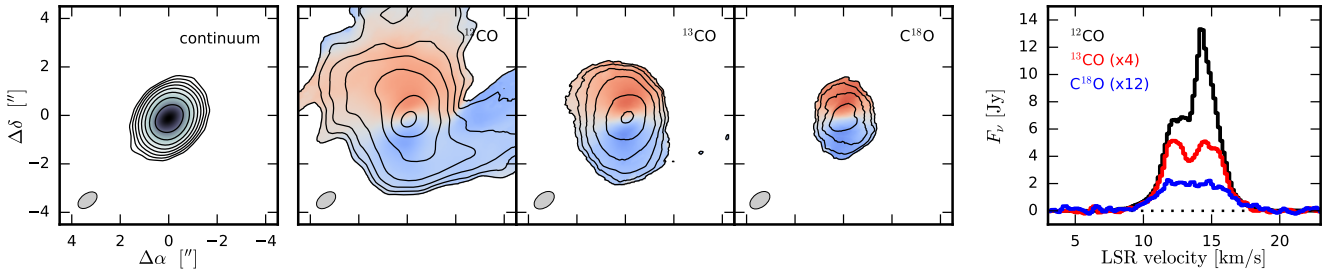


Figure 1. (left) A 226 GHz continuum image. Contours start at 5× the RMS noise level and increase by factors of 2. The synthesized beam geometry is shown in the lower left corner. (middle, left to right) Maps of the ^{12}CO , ^{13}CO , and C^{18}O velocity-integrated intensities (contours, starting at 10, 3, and 3× the RMS noise levels, respectively, and increasing by factors of 2) overlaid on the intensity-weighted projected velocities (color-scale). Note the prominent molecular cloud contamination in the ^{12}CO map (see also Fig. 2). (right) Spatially integrated spectra (inside the same CLEAN mask, and smoothed with an 0.85 km s $^{-1}$ Hanning kernel) for each CO line.

centered on the GW Ori stellar system, with a peak intensity of 67 mJy beam $^{-1}$ ($\text{S/N} \approx 1200$). Our integrated flux density measurement is consistent with that of Mathieu et al. (1995, 255 ± 60 mJy), but marginally discrepant with that of Fang et al. (2017, 320 ± 64 mJy). A crude estimate of the emission geometry (from a Gaussian fit to the visibilities) suggests an inclination of $35\text{--}40^\circ$ from face-on, with the major axis oriented $\sim 170^\circ$ E of N.

The CO isotopologue channel maps reveal bright (integrated intensities of 41.8, 5.7, and 0.8 Jy km s $^{-1}$ for ^{12}CO , ^{13}CO , and C^{18}O , respectively) and extended (FWHM $\sim 2''.5$) emission that is clearly in rotation around the continuum centroid, spanning a projected velocity range of ± 5 km s $^{-1}$ from the line center. The line emission is blueshifted to the south and redshifted to the north, consistent with the orientation estimated from the continuum emission. The peak intensities for each line are ~ 800 , 290, and 55 mJy beam $^{-1}$ in the brightest channels (peak S/N ≈ 130 , 35, and 14) for CO, ^{13}CO , and C^{18}O , respectively. The CO channel maps show some clear evidence for structured contamination from the surrounding molecular cloud, particularly as a streamer to the west at LSRK velocities $\sim 11\text{--}13$ km s $^{-1}$ and some diffuse clumps to the north around 13–14 km s $^{-1}$, confirming the “tail”-like structure seen by Fang et al. (2017). These features are much fainter, but still present, in ^{13}CO emission; they are not apparent in the C^{18}O maps.

2.2. Optical Spectroscopy

GW Ori was monitored spectroscopically at the Harvard-Smithsonian Center for Astrophysics for more than 35 years, beginning in 1981 November. A total of 203 usable spectra were gathered through 2009 April using three nearly identical echelle spectrographs (Digital Speedometers, DS; now decommissioned) with a resolving power of $R \approx 35,000$ mounted on three dif-

ferent telescopes: the 1.5m Tillinghast reflector at the Fred L. Whipple Observatory (Mount Hopkins, AZ), the 4.5m-equivalent Multiple Mirror Telescope (also on Mount Hopkins) before conversion to a monolithic mirror, and occasionally on the 1.5m Wyeth reflector at the Oak Ridge Observatory (in the town of Harvard, MA). Each instrument was equipped with an intensified photon-counting Reticon detector limiting the output to a single echelle order 45 Å wide, which was centered on the region of the Mg I b triplet at 5187 Å (see Latham 1992). The signal-to-noise ratios of these observations range from 14 to 59 per resolution element of 8.5 km s $^{-1}$, with a median of 41. Wavelength calibrations were based on exposures of a Thorium-Argon lamp taken before and after each science exposure. Reductions were performed with a dedicated pipeline, and the zero-point of the velocities was monitored regularly by means of exposures of the evening and morning twilight sky. The original analysis of Mathieu et al. (1991) used a subset of 45 of these spectra. A further 79 usable spectra of GW Ori were collected with the Tillinghast Reflector Echelle Spectrograph (TRES; Fűrész 2008), a bench-mounted, fiber-fed echelle instrument attached to the 1.5m Tillinghast reflector and providing a resolving power of $R \approx 44,000$, delivering 51 orders covering the wavelength interval 3900–9100 Å. These observations were made between 2010 November and 2017 April. Signal-to-noise ratios at 5200 Å range from 28 to 195 per resolution element of 6.8 km s $^{-1}$, with a median of 74. Wavelength calibration was carried out as above, and reductions were performed as described by Buchhave et al. (2010). Radial-velocity standard stars were observed each night to monitor the zero point and place it on the same system as the DS observations to within ~ 0.1 km s $^{-1}$.

All of our spectra appeared initially to be single-lined, with broad features indicative of significant rotation. Preliminary radial-velocity measurements were

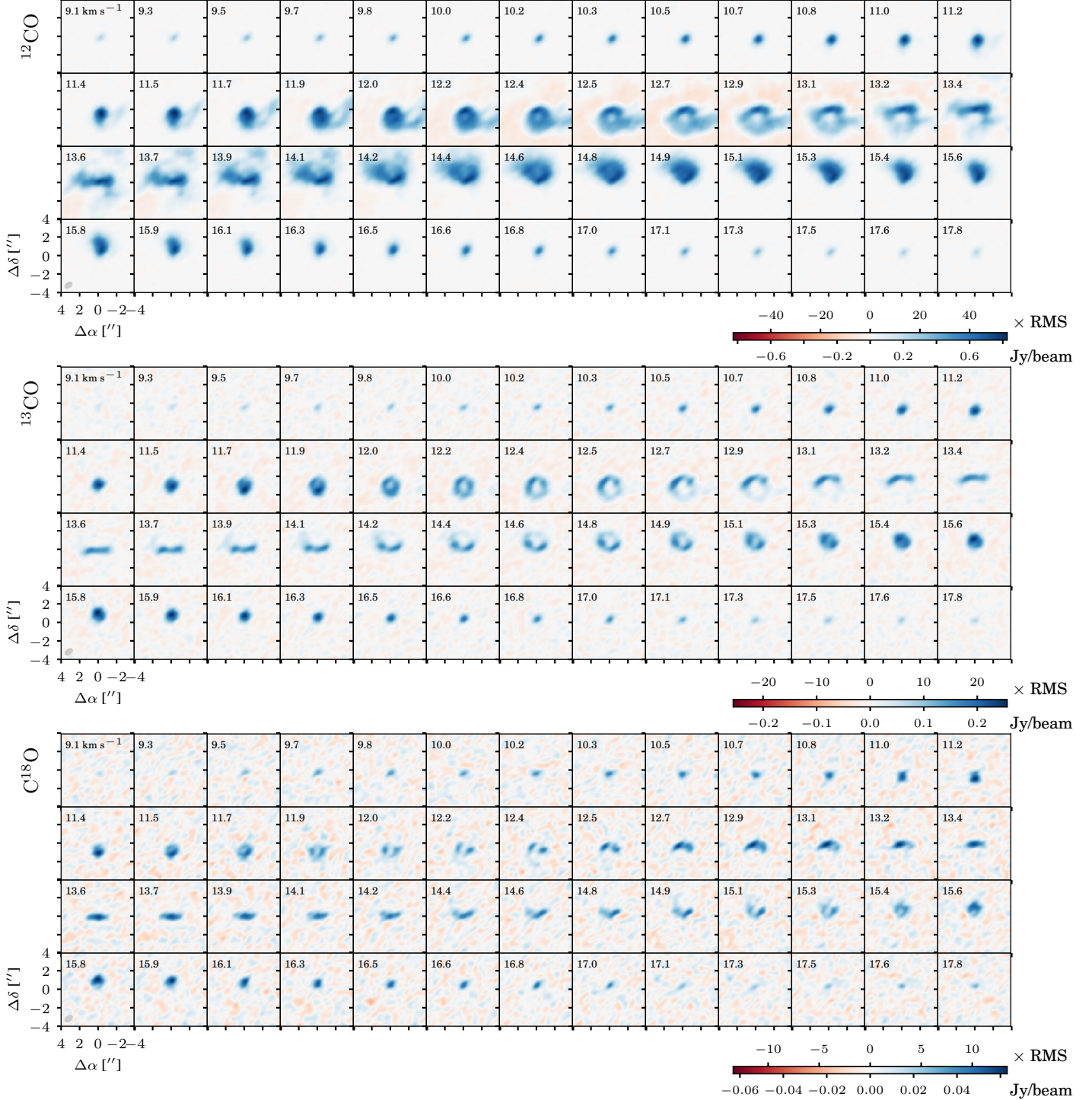


Figure 2. Channel maps of the ^{12}CO , ^{13}CO , and C^{18}O (*from top to bottom*) line emission from the GW Ori disk. Each channel represents the emission in a 170 m s^{-1} -wide velocity bin. LSRK velocities are indicated in the upper left, and synthesized beam sizes in the lower left, or each panel. Scale bars are provided at the bottom right of each set of channel maps.

therefore made with standard one-dimensional cross-correlation techniques, as in the analysis of Mathieu et al. (1991). However, several pieces of evidence suggested it should be possible to detect the lines of the secondary in the 240 day binary. In particular, the fairly

large flux ratio of $f_B/f_A = 0.57 \pm 0.05$ (weighted average) reported by Berger et al. (2011) in the H -band, when translated to the optical, would still be significant for any reasonable assumption on the temperatures of the stars, making our non-detection of the secondary

somewhat surprising. Furthermore, those same authors proposed that the system is observed nearly face-on, which would lead to strong line blending that could explain our lack of detection despite the sizable brightness of the secondary. Additionally, our efforts to disentangle the spectra described later (§3.4) indicated the primary and secondary are indeed separable. Finally, we learned of a detection by others of double lines in targeted high-resolution near-infrared spectra of GW Ori (L. Prato, private communication).

Based on these indications we re-examined our spectra with TODCOR, a two-dimensional cross-correlation algorithm designed to minimize biases in the radial velocities due to line blending, and succeeded in detecting the secondary. As anticipated, the lines of the two stars are always heavily blended, which causes a strong degeneracy between the adopted rotational line broadening for the templates (see below), the velocity amplitudes, the adopted temperatures, and the flux ratio. To measure radial velocities we adopted synthetic templates for the primary and secondary from the PHOENIX library of [Husser et al. \(2013\)](#), broadened to match the resolution of our spectra. For the TRES observations we restricted our analysis to the 100 Å order centered on the Mg I β triplet, both for consistency with the analysis of the DS spectra, which cover only a 45 Å window centered on this region, and because experience shows that it contains most of the information on the velocities. The one-dimensional cross-correlations needed to construct the 2-D correlation function in TODCOR were computed using the IRAF¹ task XCSAO ([Kurtz & Mink 1998](#)). The template parameters were selected based on an analysis of the stronger TRES spectra, as follows. For the primary star we adopted a temperature of $T_{\text{eff}} = 5700$ K proposed by [Mathieu et al. \(1991\)](#), along with $\log g = 3.0$ and solar metallicity, although the latter has minimal effect. The same composition and surface gravity were used for the secondary. The rotational broadening ($v \sin i$) of the primary, the secondary temperature, and the secondary $v \sin i$ were then determined by running extensive grids of 2-D cross-correlations over broad ranges in each parameter in a manner similar to that described by [Torres et al. \(2002\)](#), seeking the best match as measured by the peak cross-correlation coefficient averaged over all exposures. For each combination of template parameters we also determined the flux ratio that maximizes the correlation.

¹ IRAF is distributed by the National Optical Astronomy Observatories, which are operated by the Association of Universities for Research in Astronomy, Inc., under cooperative agreement with the National Science Foundation.

In this way we determined a best-fit secondary temperature of $T_{\text{eff}} = 4800 \pm 200$ K, and $v \sin i$ values for the primary and secondary of 40 and 45 km s $^{-1}$, respectively, with estimated uncertainties of 5 km s $^{-1}$. The measured flux ratio in the Mg I β 5187 Å region is $f_B/f_A = 0.25 \pm 0.05$. While in principle these temperatures and $v \sin i$ values are merely free parameters that provide the best match to the observed spectra, in the following we interpret them also as estimates of the physical properties of the stars. The radial velocities we measured from our DS and TRES spectra with these parameters are reported in Table 2, along with their uncertainties. Typical errors for the primary and secondary are 1.0 and 2.7 km s $^{-1}$ for TRES, and 2.5 and 8.7 km s $^{-1}$ for the DS measurements. Despite the use of TODCOR, we reiterate that the severe line blending at all phases of the inner orbit caused by a combination of rotational broadening and small velocity amplitudes makes the radial velocities very susceptible to errors in the template parameters (particularly $v \sin i$) and in the adopted flux ratio, and as a result the orbital elements presented later may suffer from systematic errors not included in the statistical uncertainties. Nevertheless, as a consistency check we used PHOENIX spectra from [Husser et al. \(2013\)](#) for the primary and secondary stellar parameters given above to extrapolate our measured flux ratio at 5187 Å to the near infrared, and obtained an H -band value of $f_B/f_A = 0.57 \pm 0.12$. While less precise than the [Berger et al. \(2011\)](#) measurement, the agreement is excellent.

2.3. Time-series Photometry

We have assembled a \sim 30 year high cadence lightcurve of GW Ori by drawing from several ongoing photometric surveys as well as archival observations. In this section we present the sources of our photometric data and their reduction.

2.3.1. Maidanak Observatory

Text from Grankin.

2.3.2. KELT

The Kilodegree Extremely Little Telescope (KELT) project uses two telescopes to survey over 70% of the entire sky searching for transiting planets around bright stars ($8 < V < 11$). The telescopes, located in Sonoita, AZ (KELT-North) and Sutherland, South Africa (KELT-South), have a 42mm Mamiya 645-series wide-angle lens resulting in a $26^\circ \times 26^\circ$ field-of-view (FOV), and a $23''$ pixel scale. Both telescopes use a broad R -band filter. KELT observes using a paramount ME German equatorial mount with a 180° meridian flip; therefore KELT observes in either a “east” or “west” orientation. The

Table 2. Heliocentric radial-velocity measurements of GW Ori.

HJD (2,400,000+)	RV_A (km s $^{-1}$)	σ_A (km s $^{-1}$)	RV_B (km s $^{-1}$)	σ_B (km s $^{-1}$)	ϕ_{in}	ϕ_{out}
44919.0042	31.24	5.40	28.50	19.13	0.2925	0.8663
45301.8865	25.10	5.18	25.29	18.35	0.8781	0.9572
45336.7941	23.46	3.36	20.37	11.92	0.0226	0.9655
45708.7038	33.05	5.83	20.37	20.65	0.5628	0.0538
45709.6058	37.70	2.76	25.18	9.77	0.5665	0.0540

NOTE—Observations up to HJD 2,454,926.6573 were obtained with the DS, and the remainder with TRES. Phases in the inner and outer orbits are represented with ϕ_{in} and ϕ_{out} . This table is available in its entirety in machine-readable form.

telescope optics are not perfectly axisymmetric, and so the point spread function (PSF) changes from one orientation to the other. Throughout the data reduction process, the east and west observations are treated as though they were acquired from separate telescopes. See Siverd et al. (2012) and Kuhn et al. (2016) for a detailed description of the KELT observing strategy and reduction process. GW Ori was located in KELT-South field 05 ($\alpha = 06\text{hr } 07\text{m } 48.0\text{s}$, $\delta = +3^\circ 00' 00''$) and was observed 2889 times from UT 2010 February 28 until UT 2015 April 09, with a median error of 0.005 mag.

2.3.3. ASAS

Using two observing location, in Las Campanas, Chile and Haleakala, Maui, the All-Sky Automated Survey (ASAS) project was designed to observe the entire sky to a limiting optical magnitude of 14. The two observatory setups each contained a wide-field Minolta 200/2.8 APO-G telephoto lenses with a $2\text{K} \times 2\text{K}$ Apogee CCD and both observed simultaneously in B - and V -band. The telescope and camera set up correspond to a $8.8^\circ \times 8.8^\circ$ field-of-view. ASAS observed GW Ori in the V -band from UT 2001 March 11 until UT 2009 November 29, obtaining 480 observations with a median per-point error of 0.036 mag.

2.3.4. ASAS-SN

Focused on the discovery and characterization of SuperNovae, the the All-Sky Automated Survey for SuperNovae (ASAS-SN, Shappee et al. (2014)) surveys the entire sky down to $V \sim 17$ mag every ~ 2 days. Hosted by the Las Cumbres Observatory (LCO) at Mount Haleakala, Hawaii and the Cerro Tololo Inter-American Observatory (CTIO) in Chile, each location hosts four 14-cm Nikon telephoto lenses with a $2\text{k} \times 2\text{k}$

thinned CCD (Brown et al. 2013). The telescopes have a 4.5×4.5 degree field-of-view and a $7.^{\prime}8$ pixel scale. ASAS-SN obtained 799 observations of GW Ori from UT 2014 December 16 until UT 2017 March 15, with a typical per point error of 0.01 mag.

3. ANALYSIS AND RESULTS

3.1. A Reconstruction of the Disk Velocity Field

We use the spatially and spectrally resolved molecular line emission observed with ALMA to tomographically reconstruct the disk velocity field and make a dynamical measurement of the total stellar mass. We follow the forward modeling procedures described by Czekala et al. (2015, 2016) using the associated open-source software package *DiskJockey*.²

The basis of the parametric physical model adopted in this approach is a radial surface density profile, $\Sigma(r)$, designed to mimic a simple theoretical description for a viscous accretion disk (Lynden-Bell & Pringle 1974; Hartmann et al. 1998). It decreases like $1/r$ interior to a characteristic radius R_c , and has an exponential taper e^{-r/R_c} at larger radii. The vertical distribution (z -direction) of these densities is controlled by the disk temperatures. To convert the total gas densities to molecule-specific values, we start with baseline abundances that are representative of the cold molecular interstellar medium: $[\text{H}_2/\text{gas}] = 0.8$, $^{12}\text{CO}/\text{H} = 7.5 \times 10^{-5}$, $^{12}\text{CO}/^{13}\text{CO} = 69$, and $^{12}\text{CO}/\text{C}^{18}\text{O} = 557$ (e.g., Henkel et al. 1994; Prantzos et al. 1996).

The disk kinematics are assumed to be Keplerian and dominated by the total stellar mass M_{tot} , with

² Available under an MIT license at <https://github.com/iancze/DiskJockey>.



Figure 3. A comparison of the observed channel maps of the ^{13}CO line emission (top) with a best-fit model (middle; constructed from a synthetic visibility set based on the inferred parameters listed in Table 3 and then imaged in the same way as the data) and the associated residuals (bottom; the imaged data–model residual visibilities). The annotation is the same as in Fig. 2.



Figure 4. A comparison of the observed channel maps of the C^{18}O line emission (top) with a best-fit model (middle; constructed from a synthetic visibility set based on the inferred parameters listed in Table 3 and then imaged in the same way as the data) and the associated residuals (bottom; the imaged data–model residual visibilities). The annotation is the same as in Fig. 2.

a velocity field that appropriately accounts for the two-dimensional distribution of the emitting layer (see

Rosenfeld et al. 2013). The line-spread function is characterized with a width defined by the quadrature sum

of thermal and non-thermal (ξ ; presumably turbulent) contributions. For any physical structure specified by these 6 parameters, $\{\Sigma_c, R_c, T_{10}, q, M_{\text{tot}}, \xi\}$, we solve the molecular rate equations (assuming LTE) and ray-trace the associated emission into a set of high resolution channel maps using the radiative transfer package RADMC-3D (Dullemond 2012). That ray-tracing requires that we specify 3 additional geometric parameters: the disk inclination to the line-of-sight (i_{disk}), the position angle of the disk rotation axis projected on the sky (φ), and the LSRK systemic radial velocity (v_r). Hereafter, we term this parameterization the “standard” model. The model channel maps are then Fourier transformed and sampled at the same spatial frequencies observed by ALMA. The model quality with respect to the observed visibilities is evaluated with a χ^2 likelihood function that incorporates the nominal visibility weights. We assume flat priors on all parameters except for i_{disk} , where we adopt a simple geometric prior (the disk angular momentum vector \mathbf{h}_{disk} is distributed uniformly on a sphere, e.g.; Czekala et al. 2016). We adopt a fixed distance to GW Ori of $d = 388$ pc (Kounkel et al. 2017) to make the problem more computationally tractable; we discuss the effects of this assumption in Section 3.3. The posterior distribution of these parameters is explored using Markov Chain Monte Carlo simulations with the affine invariant ensemble sampler proposed by Goodman & Weare (2010), as implemented in the emcee code (Foreman-Mackey et al. 2013) and ported to the Julia programming language, which we include in DiskJockey.

Compared to our previous similar work, the modeling of GW Ori is considerably more computationally intensive. This is primarily a consequence of the large physical size of the disk, which makes the ray-tracing step substantially more time-consuming. The inference for an individual spectral line takes $\sim 10,000$ CPU hours parallelized across 26 cores on the Harvard Odyssey Cluster. Given that restriction and the fact that the ^{12}CO line is clearly contaminated by local cloud material, we restrict our analysis to *independent* inferences of the model parameters based on the ^{13}CO and C^{18}O data only. For computational expediency we only model the data averaged to 25 channels of 0.4 km s^{-1} width. Experiments modeling a subset of the channels at higher resolution (e.g., every third channel) did not yield a significantly different result.

The inferred parameter values corresponding to the measurements of each spectral line are summarized together in Table 3. A comparison of the data and the best-fit models (and associated residuals) is presented in the form of channel maps in Figures 3 and 4 for

Table 3. Inferred Disk Model Parameters

Parameter	^{13}CO	C^{18}O
M_* [M_\odot]	5.28 ± 0.06	5.38 ± 0.23
r_c [au]	237 ± 5	151 ± 21
T_{10} [K]	51 ± 2	32 ± 4
q	0.308 ± 0.012	0.378 ± 0.037
$\log_{10} M_{\text{disk}}$	$\log_{10}[M_\odot]$	-1.69 ± 0.02
$\xi [\text{km s}^{-1}]$		0.59 ± 0.01
i_d [deg]		137.7 ± 0.3
PA ^a [deg]		90.7 ± 0.1
$v_r [\text{km s}^{-1}]$		13.651 ± 0.003
$\mu_\alpha ["]$		-0.004 ± 0.002
$\mu_\delta ["]$		-0.044 ± 0.002
		-0.051 ± 0.008

^aFor comparison with the stellar orbits, we note that the position angle of the ascending node Ω_{disk} is 90° offset from our PA convention, i.e. $\Omega_{\text{disk}} = \text{PA} + 90^\circ \approx 180.6^\circ$.

NOTE—The 1D marginal posteriors are well-described by a Gaussian, so we report symmetric error bars here.

^{13}CO and C^{18}O , respectively. While overall the models successfully reproduce the observed emission, there are some interesting residuals. Namely, an excess of emission in the center of the disk for the channels between $13.1 - 14.3 \text{ km s}^{-1}$, seen in both ^{13}CO and C^{18}O . We will return to a discussion of a potential origin in Section 4.

Motivated by the presence of the aforementioned residuals, we explored more sophisticated disk models, including a model with a vertical temperature gradient and CO depletion due to freeze-out and photodissociation (after Rosenfeld et al. 2013), as well as a flexible temperature model parameterized to mimic more sophisticated (and computationally expensive) protoplanetary disk models (Kamp & Dullemond 2004; Jonkheid et al. 2004). However, we found that neither of these models resulted in a more satisfactory fit to the data as measured by visual inspection and the Akaike information criterion (AIC). Encouragingly, however, they still yielded similar estimates of M_{tot} as the standard model, which gives us confidence that the disk-based dynamical mass is moderately robust to choice of parameterization for the temperature and density structures.

Using the standard model, the inferred physical structures inferred from each line are in mild disagreement, as might be expected for this simple parameterization. To illustrate these differences, we plot the 2D temperature

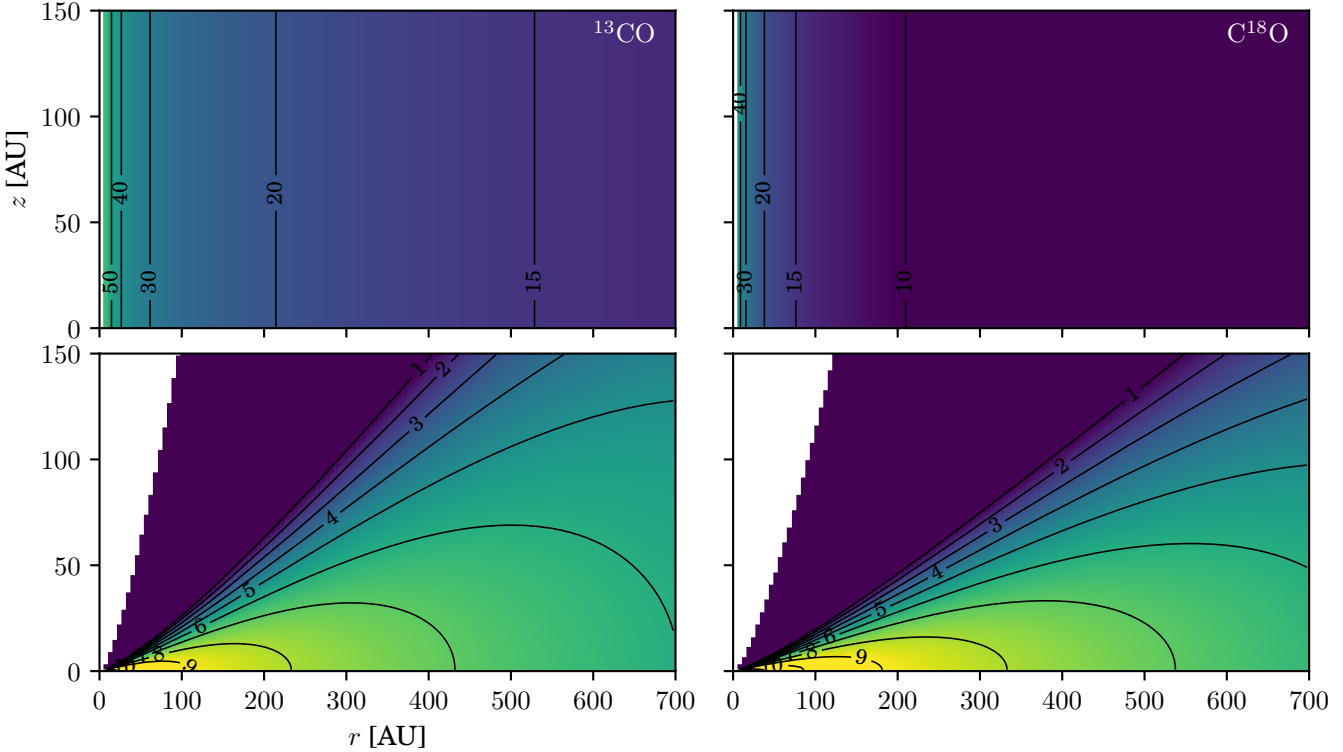


Figure 5. The maximum likelihood 2D temperature (top) and density (bottom) disk structures inferred using the ^{13}CO (left) and C^{18}O (right) transitions. The temperature contours are in units of K. The density plots show the total gas density (ρ_{gas}) and are in units $\log_{10} \text{cm}^{-3}$. The color scales are normalized to the same limits for both transitions.

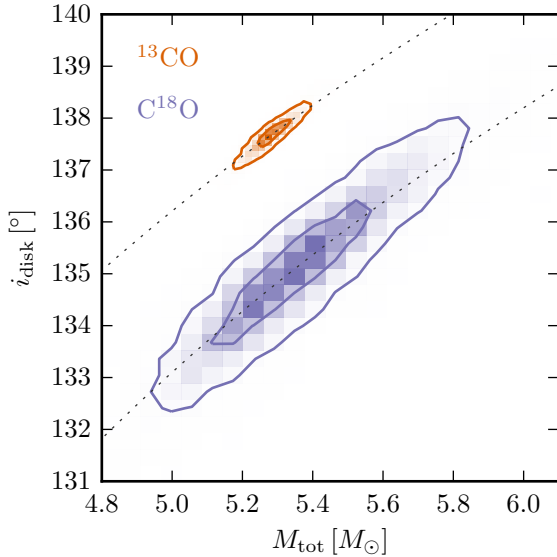


Figure 6. Posterior distributions for the model parameters fit to the ^{13}CO and C^{18}O data independently, showing 1 and 2 σ contours. Dashed lines indicate constant values of $M_{\text{tot}} \sin^2 i_{\text{disk}}$.

and density profiles inferred from each transition in Fig-

ure 5. We attribute these differences to the different layers of the disk probed by the ^{13}CO and C^{18}O transitions. In Figure 6, we plot the marginalized posteriors for both transitions in the $\{M_{\ast}, i_{\text{disk}}\}$ -plane. Interestingly, the different transitions deliver different inclinations at a statistically significant level ($\Delta i_{\text{disk}} \approx 2.5^\circ$), which we attribute to the previously mentioned model deficiencies and the fact that the ^{13}CO and C^{18}O transitions probe different layers in the disk. This difference is potentially concerning because biases in the measurement of disk inclination have the greatest potential to affect the inference of M_{tot} . With more computational power, it would be worthwhile to explore a joint fit to both transitions, to see if a single disk structure could adequately fit both transitions simultaneously. Nevertheless, both transitions yield consistent constraints on the total stellar mass, which is the most relevant parameter to our stated goals. We believe that the robustness of the dynamical mass technique is primarily because the kinematic morphology of the line emission (i.e., the location of the emission in R.A., Dec., and radial velocity space) is not strongly dependent on the exact temperature and density structure of the disk, but is rather a strong function of M_{tot} and i_{disk} , and when the disk is spatially resolved, the dependence on i_{disk} is diminished. We com-

bine the inferred total masses from ^{13}CO and C^{18}O in a weighted mean to get $M_{\text{tot}} = 5.29 \pm 0.06 M_{\odot}$. The uncertainty in the distance to GW Ori (388 ± 5 pc; Kounkel et al. 2017) linearly translates into a mass uncertainty, and so we convolve an additional 1.3% mass uncertainty with this posterior to get $M_{\text{tot}} = 5.29 \pm 0.09 M_{\odot}$, which we adopt as our reported total mass estimate. Because the inferred disk inclinations are mutually inconsistent, we adopt a weighted average for the mean inclination and assume a large systematic uncertainty, resulting in a final estimate of $i_{\text{disk}} = 137.6 \pm 2.0^\circ$. Our CO results are broadly consistent with that determined by Fang et al. (2017), who measure the disk inclination to be $\sim 35^\circ$.

3.2. An Updated Model of the Stellar Orbits

In this section, we first discuss our orbital fit to the RVs determined in §2.2, and then explore a joint RV + astrometric fit which includes the three epochs of astrometry in Berger et al. (2011). We fit a hierarchical triple orbit and solve for the elements of the inner and outer Keplerian orbits simultaneously, assuming the inner binary acts as a point mass in the outer orbit. To address possible systematic offsets present in the RV dataset, we fit for three offset terms: 1) Δv TRES, applied as a shift to all TRES RVs to account for the offset of the instrumental RV zeropoint 2) Δv_2 Reticon and 3) Δv_2 TRES, offsets which are applied to the secondary RVs to account for possible offset velocities due to template mismatch between the synthetic spectrum used as a cross-correlation template and the true spectrum of the secondary star. The residuals from our initial fit indicated our formal velocity errors are underestimated, and so the uncertainties on each data point are scaled until the final reduced $\chi^2_\nu = 1$ for our final solution.

The period of the inner orbit is consistent with that of Mathieu et al. (1991); Fang et al. (2014); however, due to the SB2 nature of the system, most other orbital parameters have significantly changed. We find a larger semi-amplitude for the primary, $K_A = 8.36 \pm 0.14 \text{ km s}^{-1}$, a mass ratio of $q \equiv M_B/M_A = 0.60 \pm 0.02$, and a statistically significant eccentricity $e_{\text{in}} = 0.13 \pm 0.02$. We find the outer orbit has an orbital period of $P_{\text{out}} = 4218 \pm 60$ days, or 11.5 years, and a statistically significant eccentricity, $e_{\text{out}} = 0.22 \pm 0.09$. We find offset terms statistically inconsistent with zero: a small but non-negligible offset between the Reticon and TRES zero-points of 0.49 km s^{-1} and larger offsets for the secondary velocities of 8.77 km s^{-1} and 6.41 km s^{-1} , for the Reticon and TRES RVs, respectively. Given the large intrinsic linewidth ($v \sin i \approx 40 \text{ km s}^{-1}$), these large offsets can reasonably be ascribed to template mismatch. All

parameters of the RV fit are listed in the first column of Table 4 and the full orbit as a function of time is shown in the second panel of Figure 7. Graphical representations of our observations and the inner and outer orbit models as a function of orbital phase are shown in Figure 8 and Figure 9, respectively.

Although there are only three epochs of published astrometry in Berger et al. (2011), these points may still considerably constrain the parameter space of possible orbits. Therefore, we explore a joint RV-astrometric analysis built upon a model of the “three-dimensional orbit” following Murray & Correia (2010), which adds new model parameters like semi-major axis, orbital inclination, and position angle of the ascending node for both inner and outer orbits. For a likelihood function, we combine the χ^2 RV likelihood and a new χ^2 likelihood for the separation and azimuth measurements of the B and C components relative to the position of A. As with the disk analysis, we also use a geometric prior on the orbital inclinations. For their last measurement epoch (2005), Berger et al. (2011) report an alternate position for the C component, and so we also perform a separate fit as if this were the true location of C. The newly constrained parameters are in the second and third columns of Table 4, and a graphical representation of the orbit is in Figure 10. With the addition of the astrometric dataset, we are able to constrain the individual stellar masses and the inclinations of the orbital planes, which are also listed in Table 4. Depending on whether the original or alternate position for C is used, we find the total stellar mass to be $M_{\text{tot}} = 5.7 \pm 0.7 M_{\odot}$ or $M_{\text{tot}} = 6.1 \pm 0.9 M_{\odot}$, respectively. Both measurements are nicely consistent with the M_{tot} independently measured by the disk-based analysis ($M_{\text{tot}} = 5.29 \pm 0.09 M_{\odot}$).

To measure the degree of misalignment between the orbital planes and the circumtriple disk, we calculate the angle Φ between the angular momentum vectors of each orbit according to Fekel (1981)

$$\cos \Phi = \cos i_1 \cos i_2 + \sin i_1 \sin i_2 \cos(\Omega_1 - \Omega_2). \quad (1)$$

We find that the mutual inclination between the disk and the inner stellar orbit is $\Phi_{\text{in}} = 44 \pm 5^\circ$ and the mutual inclination between the disk and the outer stellar orbit is $\Phi_{\text{out}} = 54 \pm 7^\circ$; these values are similar if one uses the “alternate” C position ($\Phi_{\text{in}} = 45 \pm 5^\circ$, $\Phi_{\text{out}} = 50 \pm 6^\circ$). Such a large misalignment is surprising given the naive expectation that the stellar orbits and disk would be roughly co-planar. Since these results only rest upon three astrometric epochs, however, there is a possibility that the large inferred mutual inclinations may be the result of unaccounted for systematic effects. In the next section, we use only the newly derived RVs

Table 4. Orbital elements of GW Ori.

Parameter	RV	RV + astrometry	RV + astrometry [†]
Inner orbit			
P [days]	241.49 ± 0.05	241.50 ± 0.05	241.49 ± 0.04
K_A [km s^{-1}]	8.36 ± 0.14	8.34 ± 0.15	8.36 ± 0.15
q	0.60 ± 0.02	0.60 ± 0.02	0.60 ± 0.02
a [au]	1.25 ± 0.05	1.27 ± 0.05
e	0.13 ± 0.02	0.13 ± 0.01	0.13 ± 0.01
i [deg]	157 ± 1	157 ± 1
ω_A [deg]	196 ± 7	197 ± 7	196 ± 6
Ω^b [deg]	263 ± 13	264 ± 13
T_{peri} [HJD–2,400,000]	56681 ± 4	56682 ± 4	56681 ± 4
γ [km s^{-1}]	$+28.31 \pm 0.19$	$+28.33 \pm 0.18$	$+28.29 \pm 0.19$
Δv TRES ^a [km s^{-1}]	0.49 ± 0.24	0.52 ± 0.23	0.47 ± 0.23
Δv_2 Reticon ^a [km s^{-1}]	8.77 ± 0.65	8.75 ± 0.67	8.73 ± 0.66
Δv_2 TRES ^a [km s^{-1}]	6.41 ± 0.37	6.36 ± 0.35	6.39 ± 0.39
M_A [M_\odot]	$2.80^{+0.36}_{-0.31}$	$2.94^{+0.40}_{-0.40}$
M_B [M_\odot]	$1.68^{+0.21}_{-0.18}$	$1.77^{+0.24}_{-0.24}$
Outer orbit			
P [days]	4218 ± 60	4246 ± 66	4203 ± 60
K_{AB} [km s^{-1}]	2.47 ± 0.25	2.38 ± 0.23	2.50 ± 0.24
a [au]	9.19 ± 0.32	9.15 ± 0.35
e	0.22 ± 0.09	0.13 ± 0.07	0.25 ± 0.08
i [deg]	150 ± 7	144 ± 9
ω_{AB} [deg]	307 ± 18	310 ± 21	310 ± 12
Ω^b [deg]	282 ± 9	263 ± 10
T_{peri} [HJD–2,400,000]	53560 ± 565	53911 ± 260	53878 ± 130
M_C [M_\odot]	$1.15^{+0.40}_{-0.23}$	$0.99^{+0.35}_{-0.18}$
Derived properties			
Inner time interval [cycles] ..	53.6
Outer time interval [cycles] ..	3.1
$M_A \sin i$ [M_\odot]	0.30 ± 0.02
$M_B \sin i$ [M_\odot]	0.18 ± 0.01
$M_C \sin i / (M_{\text{tot}}/M_\odot)^{2/3}$ [M_\odot]	0.22 ± 0.02
M_{tot} [M_\odot]	5.7 ± 0.7	6.1 ± 0.9

^aWe include parameters for a potential velocity offset between the primary and secondary radial velocities for each instrument. In principle, this term should be consistent with 0; the non-zero value likely indicates that there is some moderate template mismatch between the secondary stellar spectrum and the synthetic spectrum used as a cross correlation template.

^bWe follow the convention of the visual binary field and define the ascending node as the line of nodes where the secondary component (e.g., star B for the inner orbit, and star C for the outer orbit) crosses the plane of the sky moving *away* from the observer.

[†]Fit using the “alternate” C position for the 2005 epoch of astrometry in Berger et al. (2011).

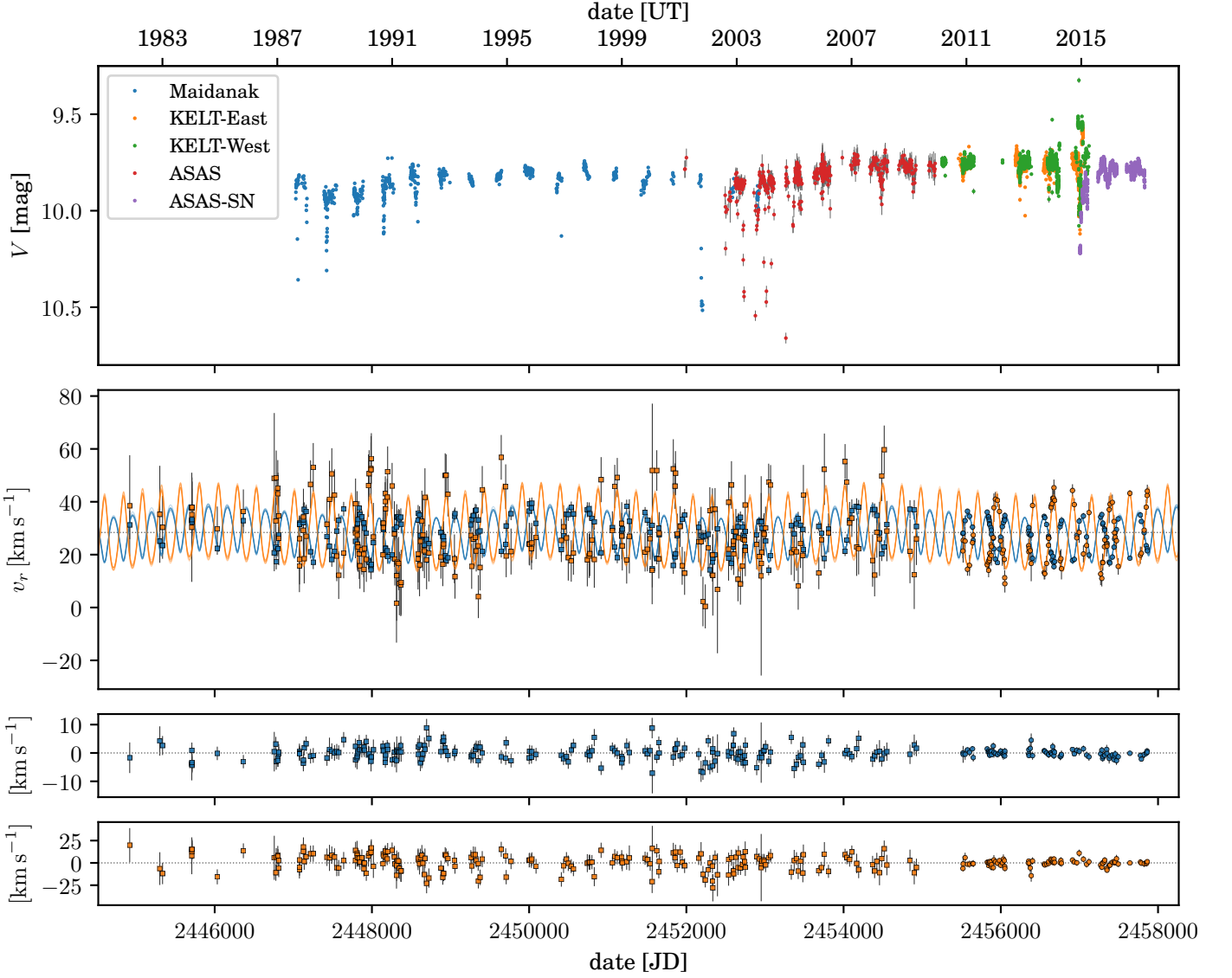


Figure 7. *top:* photometric observations of GW Ori from 1987 until mid 2017. All photometric observations displayed here are in the V -band (ASAS, ASAS-SN, and Maidanak) or a broader filter (KELT) which has been shifted to align with V -band where the time series overlap. *bottom:* primary (blue) and secondary (orange) radial velocities overlaid with several realizations of the most probable orbits, to show uncertainty in the orbit. Reticon velocities are shown with squares, TRES velocities are shown with circles, and the dotted line represents the center-of-mass velocity. Residuals for this orbit are shown in the panels below.

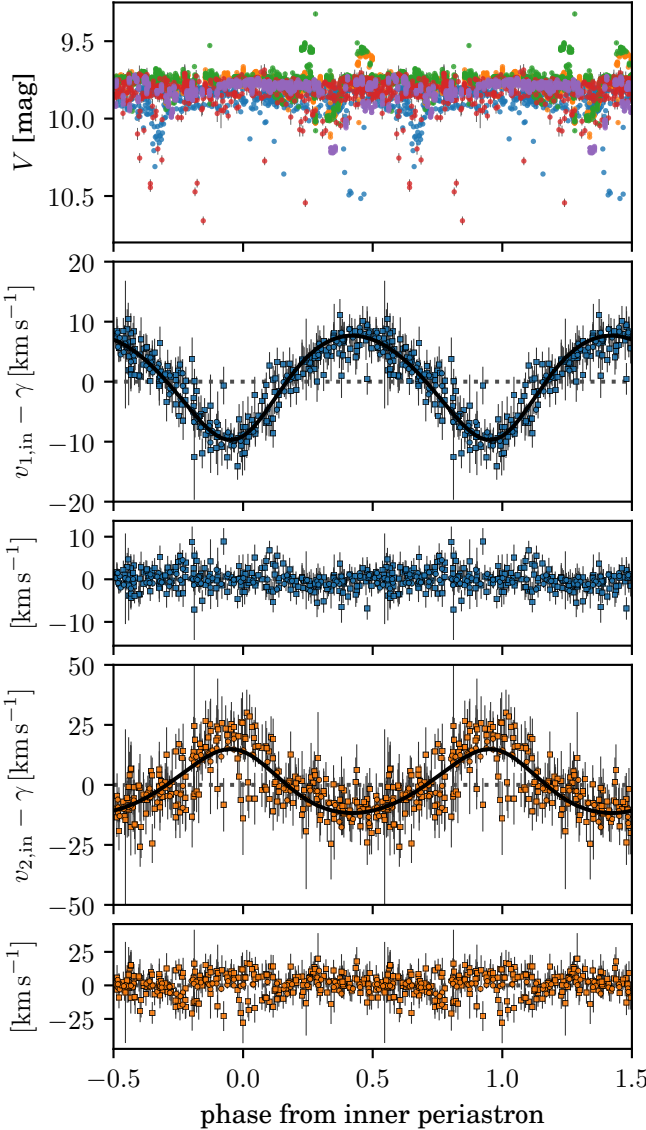


Figure 8. *top:* V -band light curve phased to the inner orbital period. No discernible correlation is detected. *bottom:* RV measurements of GW Ori and best-fit model for the inner orbit, after subtracting the motion due to the outer orbit.

and disk inclination to formulate a more conservative estimate of the mutual inclinations. We advocate continued astrometric monitoring of the GW Ori system to further improve the three-dimensional orbit and definitively confirm the inclinations of the stellar orbits.

3.3. Joint Radial Velocity and Disk Constraints on Individual Component Masses

In this section, we combine the double-lined RV constraints with the disk-based constraints on the total stellar mass to form an independent constraint on the individual stellar masses of the GW Ori system with-

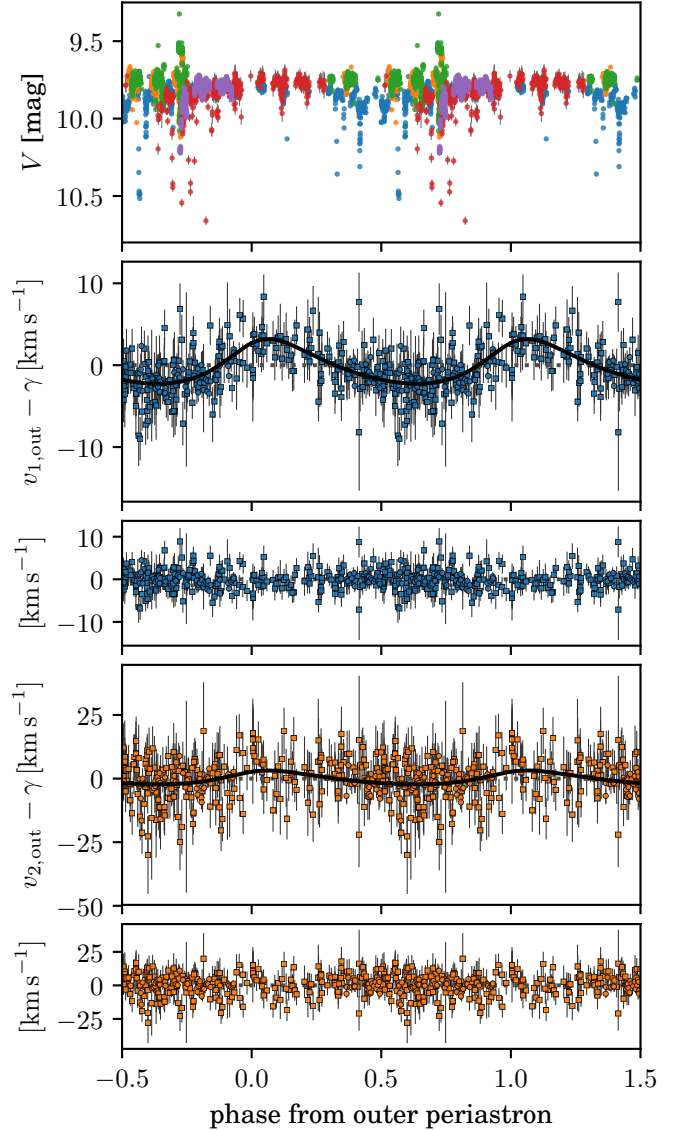


Figure 9. *top:* V -band light curve phased to the outer orbital period, showing an emerging trend that dimmings and eclipse events tend to cluster near and after apoastron ($\sim 0.4 - 0.8$). *bottom:* RV measurements of GW Ori and best-fit model for the outer orbit, after subtracting the motion due to the inner orbit.

out referencing the Berger et al. (2011) astrometry. We construct a joint likelihood function with the following five parameters: M_A , M_B , M_C , i_{in} , and i_{out} . The double-lined radial velocity constraints are sufficiently captured by the summary statistics $M_A \sin^3 i_{in}$, $M_B \sin^3 i_{in}$, $M_C \sin i_{out} / (M_{\text{tot}}/M_{\odot})^{2/3}$ and the covariances between them, which are well represented by

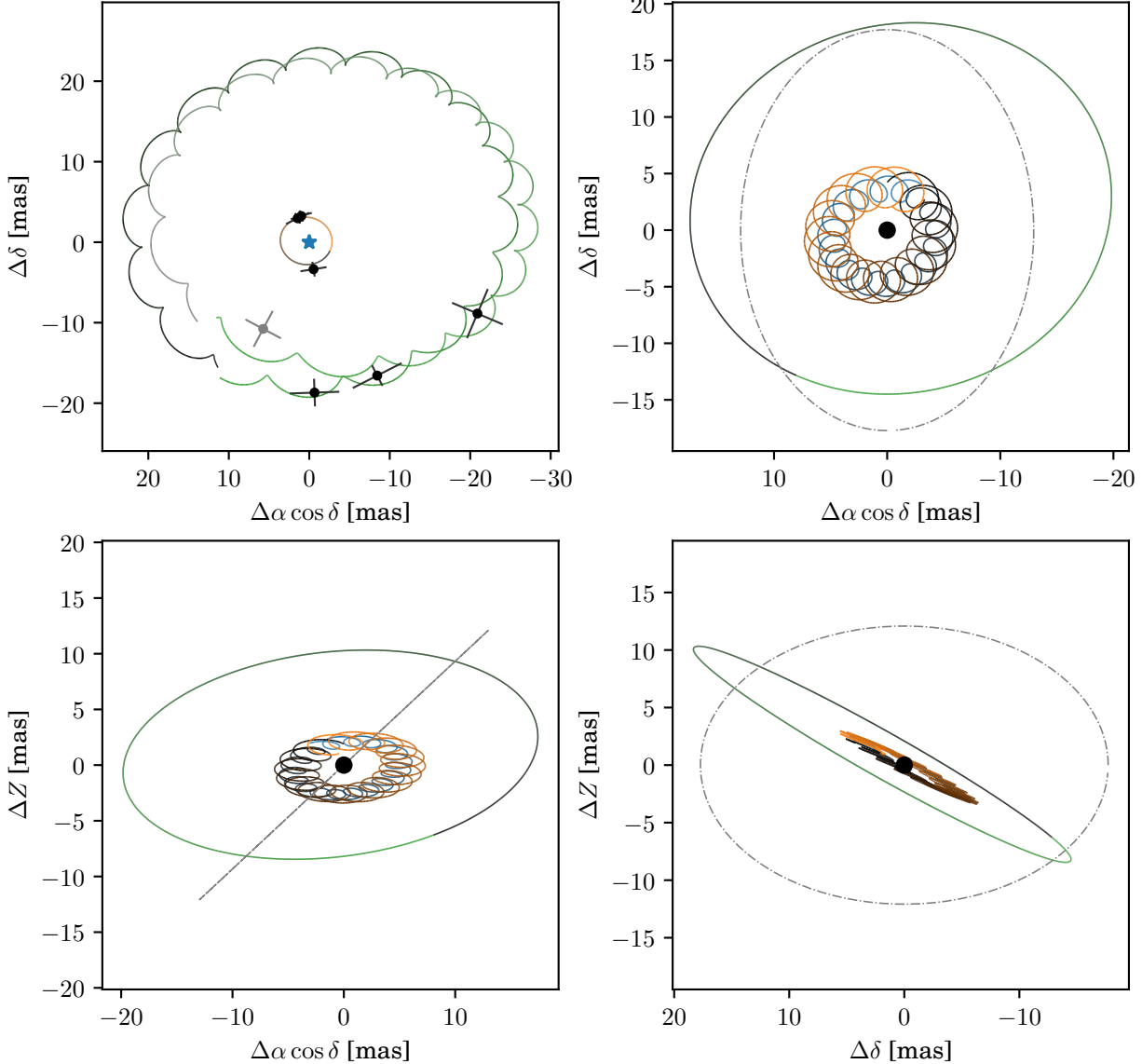


Figure 10. Orbits from the joint RV-astrometric fit shaded according to their phase, where black represents periastron and color hue increases with orbital phase. *top left:* orbits relative to the primary star A, in the plane of the sky, with the three epochs of astrometry from Berger et al. (2011). The light grey data point and outer orbit represent the fit to the “alternate” position for C. The following plots are relative to the center of mass of the system, and a fictitious particle on a circular orbit coplanar with the circumtriple disk at 7 au is shown as grey dashed line. *top right:* the sky plane *bottom left:* looking down the North axis *bottom right* looking down the East axis. Positive Z points towards observer.

a multivariate Gaussian distribution.³ The disk constraint on the total stellar mass M_{tot} is well-represented by a Gaussian, as well. We enforce flat priors on the stellar masses and geometrical priors on the inclinations. We use the ensemble sampler MCMC (Goodman

& Weare 2010; Foreman-Mackey et al. 2013) with 20 walkers to explore the posterior for 50,000 iterations, burn 25,000 iterations, and assess convergence by ensuring the Gelman-Rubin statistic (Gelman et al. 2014) is $\hat{R} < 1.1$ for all parameters.

This analysis produces consistent but less precise constraints on the stellar masses as the joint RV + astrometric fits (see Table 5). Like the RV + astrometric analysis, the disk + RV analysis also indicates that the inner stellar orbit must be significantly misaligned with the disk,

³ Note that we do not use additional constraints on q_{in} or other derived parameters, as this would amount to double-counting the RV constraints.

Table 5. Joint constraints on stellar masses and orbital inclinations

Parameter	RV + astrometry	RV + disk
$M_A [M_\odot]$	$2.80^{+0.36}_{-0.31}$	$2.74^{+0.15}_{-0.52}$
$M_B [M_\odot]$	$1.68^{+0.21}_{-0.18}$	$1.65^{+0.10}_{-0.31}$
$M_C [M_\odot]$	$1.15^{+0.40}_{-0.23}$	$0.88^{+0.85}_{-0.19}$
i_{in} [deg]	157^{+1}_{-1}	151^{+1}_{-2}
i_{out} [deg]	150^{+7}_{-7}	130^{+28}_{-27}

NOTE—The RV + astrometry values are replicated from Table 4 for comparison purposes. We note that we are not able to infer the absolute inclination of the stellar orbits directly from the radial velocity data, so there is in fact an alternate solution for the RV + disk results that yields $i_{\text{alt}} = 180^\circ - i$. This solution would be inconsistent with the astrometric motion, however, so we opt to only report the solutions with $i \geq 90^\circ$.

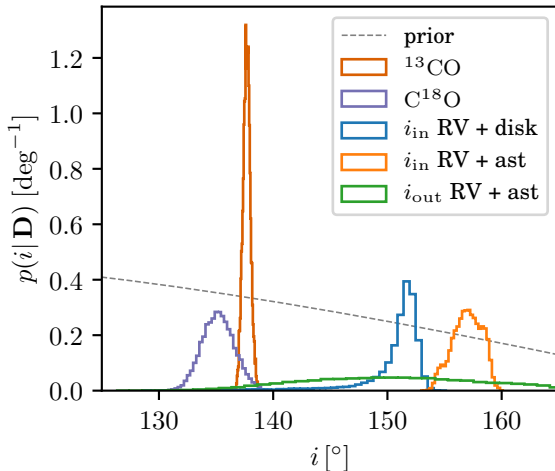


Figure 11. The inclination posteriors on the disk inclination, inner stellar orbit, and outer stellar orbit, as determined from various joint fits. Because i_{out} is essentially unconstrained by the RV + disk analysis, it is not plotted for aesthetic reasons. The geometric prior on inclination (uniform orientation of orbits in 3D space) is shown as a thin grey dotted line.

although the true misalignment is unknown since the difference between i_{in} and i_{disk} only provides a lower limit on the mutual inclination because the true mutual inclination must consider the position angles of the orbits as well. To highlight these findings, we overplot our newly derived constraints on the disk inclination and the stellar orbits in Figure 11. At the lowest inclinations (nearest

to edge-on, $i = 90^\circ$) are the measurements for the disk in ^{13}CO and C^{18}O . This is commensurate with the disk inclination measurements from Fang et al. (2017), and so we consider these results to be robust. Interestingly, the constraints on i_{in} differ between the RV + astrometry and the RV + disk results at a significant level. We speculate that this difference might be due to unknown systematics in the astrometry or RV datasets, or potentially an error in our assumption of the distance to GW Ori. While the astrometry + RV analysis does not require a distance to the source, the disk-based analysis does require a distance in order to break the M_{tot}/d degeneracy. Although the exact degree of mutual inclination between the inner orbit and the disk is unknown, we conclude that it is likely that it is at least 10° and potentially as high as 45° . The RV + disk constraints on the outer orbit are less precise, but also suggest that the planes are at least somewhat misaligned.

3.4. Disentangling the GW Ori Double-lined Spectroscopic Binary

As we noted in §2.2, at optical wavelengths GW Ori clearly appears to be a *single-lined* spectroscopic system, despite full coverage of the 240 day inner period at moderate to high S/N (Mathieu et al. 1991; Fang et al. 2014). In this context, the Berger et al. (2011) H-band detections of the secondary and tertiary stars at favorable flux ratios ($f_B/f_A = 0.57 \pm 0.05$ and $f_C/f_A = 0.23 \pm 0.01$) were rather puzzling, since such a bright secondary companion should have detectable optical signatures. We originally embarked on a search for these signatures using the then-under-development PSOAP spectroscopic disentangling package (Czekala et al. 2017), with a strong assumption that these spectral signatures must be at or near the detection limit (e.g., $q_{\text{in}} \lesssim 0.2$), since they had not been seen in previous analyses. Our preliminary results hinted at the detection of a secondary spectrum, but with mass ratios much larger than what we had expected ($q_{\text{in}} > 0.5$). Because the algorithm was still under development, we discounted these initial results as spurious and possibly the result of contamination by stellar variability. To our excitement, however, shortly thereafter we learned that GW Ori had been revealed as a *double-lined* spectroscopic binary using targeted high resolution infrared spectroscopy ($q_{\text{in}} \sim 0.65$, L. Prato, private communication, March 2017). Using this knowledge, we renewed our efforts to search for the secondary signature using PSOAP and targeted T0DCOR analysis.

The PSOAP spectroscopic disentangling technique works as an inference framework. Given a time-series of high resolution spectroscopic observations covering

the orbital phase of the binary or triple star, it simultaneously infers the intrinsic spectrum of each star along with the stellar orbit. PSOAP uses Gaussian processes to model the unknown stellar spectra, providing a robust probabilistic framework by which the spectra and orbits can be inferred in a purely data-driven manner. Once disentangled, these spectra can be used to infer fundamental stellar properties by traditional analysis techniques. For more information on the mathematical details of PSOAP please consult Czekala et al. (2017). At present, one limitation of the PSOAP framework (and Gaussian processes in general, to some extent) is the heavy computational requirement for performing the matrix calculations. This generally limits us to considering less than 20 epochs of high resolution spectra at a time, which consequentially limits the complexity of the orbital model that we can use. Although it was straightforward to extend the framework to utilize a hierarchical triple orbital model and three Gaussian process components, we found that we were unable to employ enough spectroscopic epochs to sufficiently constrain the more complex orbital model. Therefore, we experimented using different subsets of the data to test our sensitivity to presence of secondary and tertiary spectral signatures. In all of these tests, we clearly detected the features of the secondary but found no solid evidence for spectroscopic signatures of the tertiary. We have identified possible avenues of development to expand the number of spectroscopic epochs under consideration, but exploring these options will require development and testing beyond the scope of this paper.

While PSOAP unfortunately has a limited ability to constrain the orbital parameters of GW Ori, it can still provide disentangled spectra of the primary and secondary stars. To work around the epoch limit, we selected the 16 highest SNR spectra in the narrow date range of JD 2455826 to 2456052, which covers $\sim 95\%$ of the inner orbital period and both quadrature phases while being minimally sensitive to the longer term radial velocity trend due to the tertiary. To converge the binary orbital model to an adequate set of orbital parameters, we use 40 Å of spectra containing many deep absorption lines between 5160 and 5200 Å broken up into 5 Å chunks. We note that this set of orbital parameters (which we do not report) is likely incorrect given the triple nature of the system, but since we used a narrow range of data, the predicted radial velocities of the primary and secondary should be sufficiently accurate. Using this set of orbital and Gaussian process parameters, we disentangle a wider wavelength range of data covering 5060 - 5310 Å. This overlaps with the wavelength range of a tuned CfA version of the Kurucz

models, which has been used for extensive radial velocity analysis and is tuned for solar-like stars (Buchhave et al. 2012). The disentangled spectra are shown in Figure 12, overlaid with two representative Kurucz models of XX and XX.

In general, an inherent limitation of disentangling techniques is that they are unable to provide any information on the flux ratios of the components: they are only able to provide the relative amplitudes of the spectral variations. Essentially, there emerges a degeneracy between a bright companion star with shallow spectral lines and a faint companion star with deep spectral lines. Therefore, in order to re-normalize⁴ the disentangled spectra to compare with synthetic models, we must assume a flux ratio between the two stars. In light of this, the process of inferring stellar parameters becomes rather difficult, especially since both GW Ori A and GW Ori B may suffer from veiling and both the re-normalization and veiling affect the “contrast” level of the spectra. Over this narrow wavelength range, T_{eff} mainly changes the depth of the lines, while $\log g$ and $v \sin i$ mainly change the shape and depth of the lines. Therefore, the parameters we report are merely one of many possible best fit solutions; in reality, the stellar parameters could plausibly range by $\Delta T_{\text{eff}} \sim 500$ K, $\Delta \log g \sim 0.5$ dex, and $\Delta v \sin i \sim 10 \text{ km s}^{-1}$ in a correlated manner for each star, especially given uncertainties about the flux ratio and veiling.

3.5. Photometric Analysis

Using the Lomb-Scargle (LS) periodicity search algorithm (Lomb 1976; Scargle 1982) within the VARTOOLS analysis package (?), we searched for periodic variability in the high cadenced KELT observations. Specifically, we remove the eclipses shown in Table 13 from the KELT data and searched for a periodic signal from 1.1 to 100 days. The top two periods we recover are 74.798 and 2.931 days. See Figure 13 for the phase-folded lightcurves. Additionally, we remove the KELT observations and phase the V-band observations from ASAS, ASAS-SN, and Maidanak to our derived orbital periods of 241.79 and 4121.12 days. We find no convincing coherent signal at the ~ 242 days but the photometric observations phased to the ~ 4121 day period show a coherent sinusoidal variability with a peak-to-peak amplitude of ~ 0.15 mag.

⁴ Note that this is *not* continuum normalization in the traditional sense (e.g. dividing by a spline fit to the stellar continuum), but simply a constant scaling by a ratio defined in Czekala et al. (2017, Eqn. 32) which preserves broad-scale shapes intrinsic to the spectra.

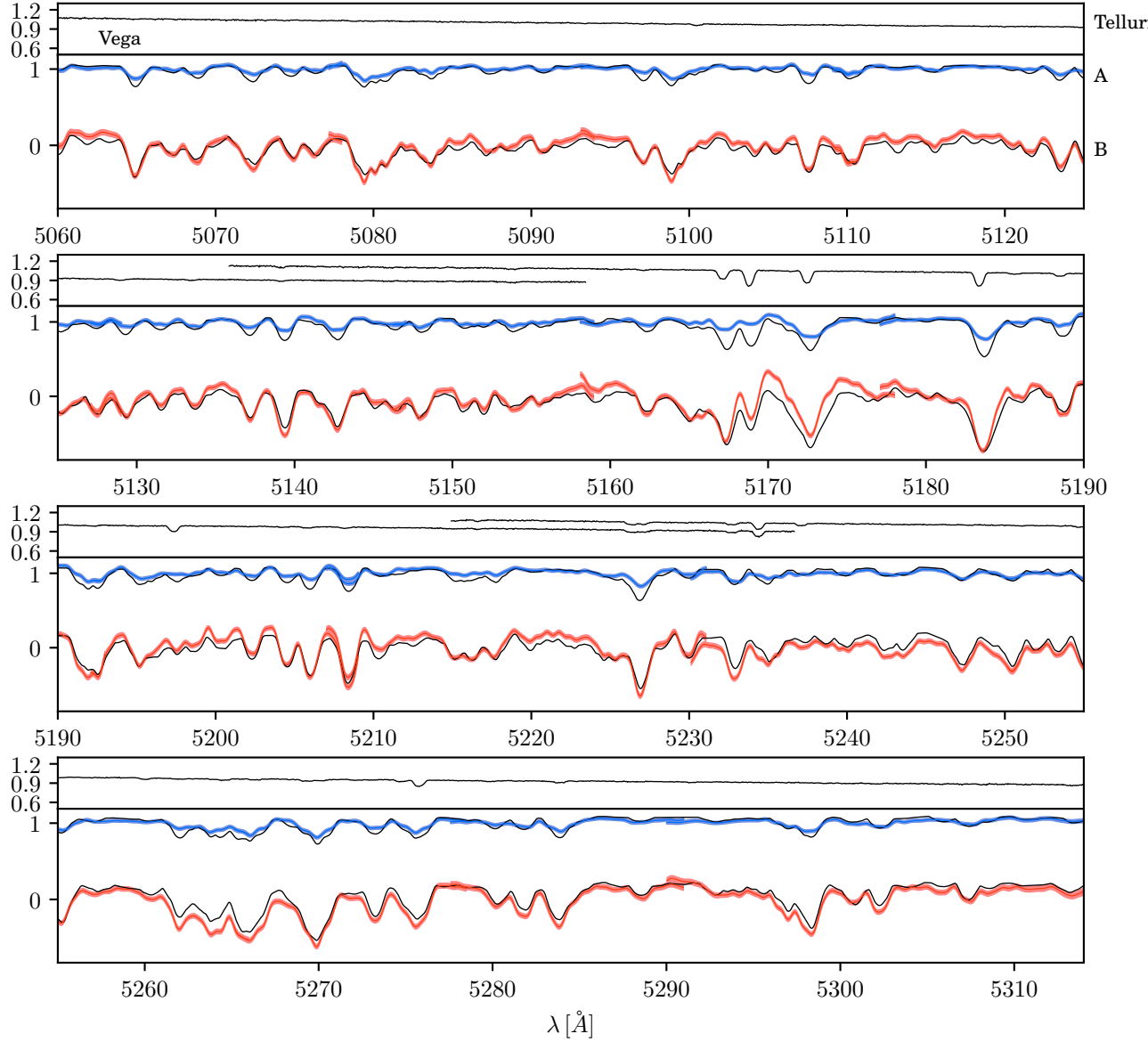


Figure 12. The disentangled spectra of GW Ori A and GW Ori B in blue and red, respectively. The top bar shows a spectrum of Vega, to demonstrate that this wavelength band is free from any telluric line contamination. The disentangled spectra have been inversely scaled by an assumed flux ratio to bring their continuum level to 1 to facilitate better comparison to the synthetic models. Disentangled spectra at the edges of echelle orders may appear jagged (e.g. $\sim 5160 \text{ \AA}$). In this figure, we have assumed $f_B/f_A = 0.43$. The overplotted synthetic models for the primary and secondary stars have stellar parameters $T_{\text{eff}} = 6000 \text{ K}$, $\log g = 3.0 \text{ dex}$, $v \sin i = 40 \text{ km s}^{-1}$ and $T_{\text{eff}} = 5000 \text{ K}$, $\log g = 3.0 \text{ dex}$, $v \sin i = 35 \text{ km s}^{-1}$, respectively.

Discussion of possible occulter size and orbital radius

4. DISCUSSION

With the disk-based and radial velocity constraints on the system architecture now established and component masses identified, we shift discussion to the photospheric properties of the stars and the age of the system. Then, we use these constraints to discuss the dynamic inner environment, given rise to by the triple nature of the

system, including the quasi-periodic nature of the photometric eclipses and pulsed accretion. Finally, we discuss the system architecture in context of other triple systems and possible formation mechanisms.

4.1. The Age and Photospheric Properties of the GW Ori Stars

Pre-main sequence evolutionary models are commonly used to infer the mass and age of young stars using measurements of their photospheric properties. We perform

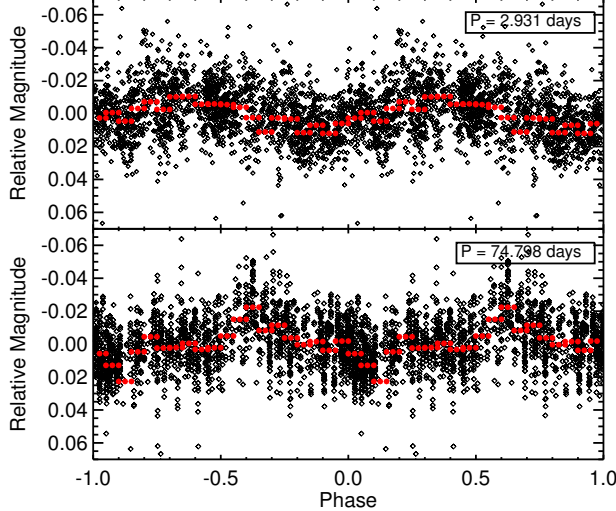


Figure 13. The KELT photometric observations of GW Ori, with the three eclipses removed, phased to the 2.931 (Top) and 74.798 (Bottom) day periods recovered from our LS analysis.

Table 6. V-band Photometric Eclipse Catalog

Start JD	End JD	Duration days	Depth mmag	Telescope
2447043	2447056	13	600	Maidanak
2447153	2447179	26	300	Maidanak
2447418	2447435	17	450	Maidanak
2447809	2447824	15	130	Maidanak
2448137	2448162	25	300	Maidanak
2448545	2448586	41	150	Maidanak
≥ 2450399	≤ 2450414	≤ 15	300	Maidanak
2452184	≥ 2452209	≥ 25	750	Maidanak
2454445	2454502	57	100	ASAS
2455507	2455535	28	60	KELT
2456212	2456248	36	110	KELT
2456709	2456742	33	150	KELT
2456989	2457032	≤ 43	≥ 250	KELT

this exercise for GW Ori A and evaluate the consistency of the model predictions with our measured dynamical mass. Due to the lingering uncertainties in the orbital constraints and thus the individual component masses, rather than evaluating the consistency of the pre-Main Sequence model predictions compared to our measured fundamental properties, instead we simply use the pre-

Main Sequence models to guide discussion about the individual component properties and assess consistency.

We adopt the luminosity constraints and extinction values of GW Ori as determined by Fang et al. (2014): $L = 48 \pm 10 L_{\odot}$ and $A_V = XX$.

We evaluate the concordance of the following pre-main sequence models: Choi et al. (2016) models, Dotter et al. (2008), Tognelli et al. (2011), and Siess et al. (2000). We cannot test the Baraffe et al. (2015) models because they do not include models with sufficiently massive stars.

We evaluate the model predictions in a Bayesian manner, following the approach in Jørgensen & Lindegren (2005); Rosenfeld et al. (2012); Czekala et al. (2015). The models deliver (among other quantities) the photospheric properties as a function of stellar mass and age, e.g., $T_{\text{eff}}(M_*, \tau)$ and $L(M_*, \tau)$. The posterior probability distribution is found by evaluating the consistency of the model predictions for a given $\{M_*, \tau\}$ with the measured photospheric properties by Fang et al. (2014), multiplied by any priors on $\{M_*, \tau\}$ (in this case, flat)⁵. The resulting posterior probability distributions are shown in Figure 14 and are listed in Table ???. In general, all four models make similar predictions about GW Ori A, $\langle M_A \rangle = 3.9 \pm 0.3 M_{\odot}$ and $\langle \tau \rangle = 0.6 \pm 0.3 \text{ Myr}$. We assess the probability of consistency between the model-predicted mass and our dynamical mass by evaluating $p(M_{\text{model}} = M_{\text{dyn}}) = \int_0^{\infty} p_{\text{model}}(M) p_{\text{dyn}}(M) dM$. For most models, the predicted stellar mass is significantly less than our measured dynamical mass, $M_A = 4.40 \pm 0.18 M_{\odot}$, and is consistent only at the 2σ level. Notably, the value of M_A predicted by our joint radial velocity and astrometric fit ($M_A = 3.72 \pm 0.32 M_{\odot}$) is in complete agreement with the model predictions. As mentioned by Fang et al. (2014), GW Ori A is likely at an earlier evolutionary stage than Herbig Be stars, although it will eventually become one.

Berger et al. (2011) modeled the H-band visibilities of the GW Ori system measured by the IOTA/IONIC3 interferometer, and measured the positions of all three GW Ori components and their flux ratios. Their mean H-band flux ratios (computed as the weighted mean of all measurements) are $f_B/f_A = 0.57 \pm 0.05$ and $f_C/f_A = 0.23 \pm 0.01$. In Figure 15, we plot the ratio of effective temperatures and the computed flux ratios in Bessell I band and 2MASS H band. Bessell I roughly corresponds to the reddest echelle orders of the TRES spectrograph that we used to search for companion spectral lines. These flux ratios are generally very small and

⁵ Our code used to perform this analysis is available under an MIT open source license here: <https://github.com/iancze/ScottiePippen>

provide an explanation for why we were unable to detect secondary or tertiary spectral lines in our searches. Moreover, this means that the excess H-band flux of the B and C components is likely due to the presence of a circumstellar disk or accretion signatures above the photospheric emission of these stars, as Berger et al. (2011) speculated. GW Ori thus presents itself as an ideal candidate for long-term high resolution infrared radial velocity monitoring to detect spectral lines from the secondary and tertiary.

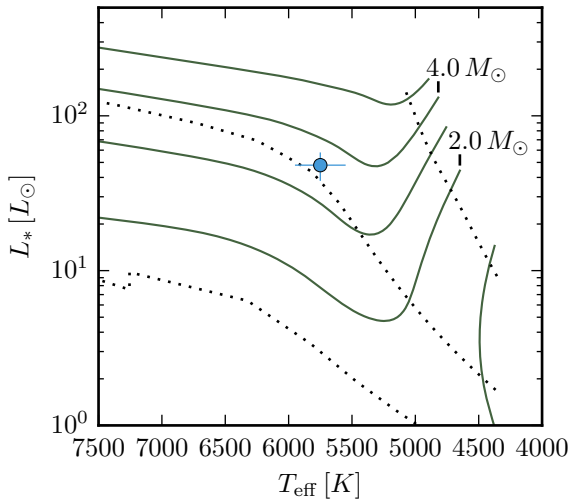


Figure 14. An HR diagram showing all three stars.

4.2. The dynamic center of the GW Ori system

4.3. The GW Ori triple system in context

5. SUMMARY AND CONCLUSIONS

- Derived a dynamical mass for GW Ori
- Derived a new SB2 orbit for the stars, and disentangled spectra
- Compared the mutual inclinations for the disk and the stellar orbits
- Evaluate the concordance between stellar properties and PMS models
- Published lightcurve w/ eclipse analysis

- Placed system in context of triple systems
- Placed system in context of dippers

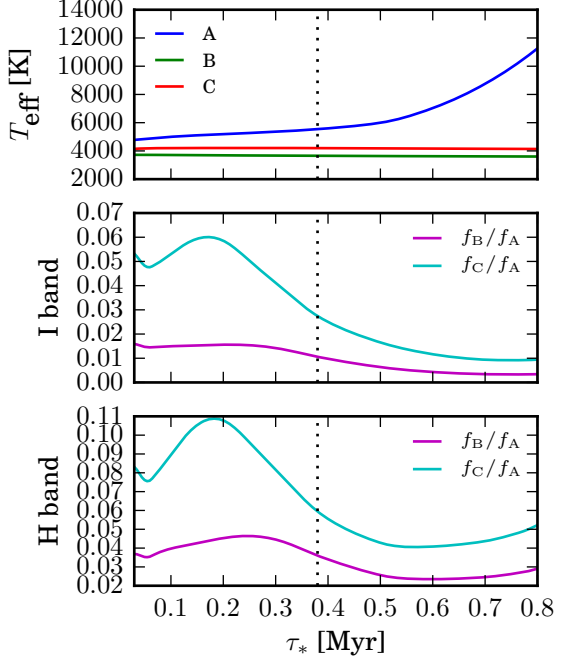


Figure 15. Relative photospheric properties of the GW Ori stellar components as a function of age, assuming they are coeval, predicted by the MIST pre-main sequence evolutionary models. *top:* The cool effective temperature of GW Ori A indicates that it must be a very young star ($\tau < 5$ Myr). The nominal age of GW Ori as predicted by the MIST models is labeled as a vertical dashed line. *middle and bottom:* the predicted flux contrasts in Bessell I band and 2MASS H, respectively.

IC acknowledges support from the Smithsonian Institution for the production of this manuscript. IC acknowledges helpful conversations with Maxwell Moe about GW Ori and related systems. SA acknowledges the very helpful support provided by the NRAO Student Observing Support program related to the early development of this project. This paper makes use of the following ALMA data: XX ALMA is a partnership of ESO (representing its member states), NSF (USA), and NINS (Japan), together with NRC (Canada) and NSC and ASIAA (Taiwan), in cooperation with the Republic of Chile. The Joint ALMA Observatory is operated by ESO, AUI/NRAO, and NAOJ. This research made extensive use of the Julia programming language (Bezanson et al. 2012) and Astropy (Astropy Collaboration et al. 2013).

REFERENCES

- Ansdell, M., Gaidos, E., Williams, J. P., et al. 2016a, *MNRAS*, **462**, L101
- Ansdell, M., Gaidos, E., Rappaport, S. A., et al. 2016b, *ApJ*, **816**, 69
- Astropy Collaboration, Robitaille, T. P., Tollerud, E. J., et al. 2013, *A&A*, **558**, A33
- Baraffe, I., Homeier, D., Allard, F., & Chabrier, G. 2015, *A&A*, **577**, A42
- Berger, J.-P., Monnier, J. D., Millan-Gabet, R., et al. 2011, *A&A*, **529**, L1
- Bezanson, J., Karpinski, S., Shah, V. B., & Edelman, A. 2012, ArXiv e-prints, [arXiv:1209.5145 \[cs.PL\]](https://arxiv.org/abs/1209.5145)
- Brown, T. M., Baliber, N., Bianco, F. B., et al. 2013, *PASP*, **125**, 1031
- Buchhave, L. A., Bakos, G. Á., Hartman, J. D., et al. 2010, *ApJ*, **720**, 1118
- Buchhave, L. A., Latham, D. W., Johansen, A., et al. 2012, *Nature*, **486**, 375
- Choi, J., Dotter, A., Conroy, C., et al. 2016, *ApJ*, **823**, 102
- Czekala, I., Andrews, S. M., Jensen, E. L. N., et al. 2015, *ApJ*, **806**, 154
- Czekala, I., Andrews, S. M., Torres, G., et al. 2016, *ApJ*, **818**, 156
- Czekala, I., Mandel, K. S., Andrews, S. M., et al. 2017, *ApJ*, **840**, 49
- Dolan, C. J. 2000, PhD thesis, Department of Astronomy, University of Wisconsin–Madison, 475 North Charter Street, Madison, WI 53706
- Dolan, C. J., & Mathieu, R. D. 2001, *AJ*, **121**, 2124
—. 2002, *AJ*, **123**, 387
- Dotter, A., Chaboyer, B., Jevremović, D., et al. 2008, *ApJS*, **178**, 89
- Duchêne, G., & Kraus, A. 2013, *ARA&A*, **51**, 269
- Dullemond, C. P. 2012, RADMC-3D: A multi-purpose radiative transfer tool, Astrophysics Source Code Library, [ascl:1202.015](https://ascl.net/1202.015)
- Fang, M., Sicilia-Aguilar, A., Roccatagliata, V., et al. 2014, *A&A*, **570**, A118
- Fang, M., Sicilia-Aguilar, A., Wilner, D., et al. 2017, *A&A*, **603**, A132
- Fekel, Jr., F. C. 1981, *ApJ*, **246**, 879
- Foreman-Mackey, D., Hogg, D. W., Lang, D., & Goodman, J. 2013, *PASP*, **125**, 306
- Fürész, G. 2008, Ph.D. Thesis, Univ. Szeged, Hungary
- Gelman, A., Carlin, J. B., Stern, H. S., et al. 2014, Bayesian data analysis, Vol. 2 (CRC press Boca Raton, FL)
- Goodman, J., & Weare, J. 2010, Communications in Applied Mathematics and Computational Science, **5**, 65
- Hartmann, L., Calvet, N., Gullbring, E., & D'Alessio, P. 1998, *ApJ*, **495**, 385
- Henkel, C., Wilson, T. L., Langer, N., Chin, Y.-N., & Mauersberger, R. 1994, in Lecture Notes in Physics, Berlin Springer Verlag, Vol. 439, The Structure and Content of Molecular Clouds, ed. T. L. Wilson & K. J. Johnston, 72
- Husser, T.-O., Wende-von Berg, S., Dreizler, S., et al. 2013, *A&A*, **553**, A6
- Jonkheid, B., Faas, F. G. A., van Zadelhoff, G.-J., & van Dishoeck, E. F. 2004, *A&A*, **428**, 511
- Jørgensen, B. R., & Lindegren, L. 2005, *A&A*, **436**, 127
- Kamp, I., & Dullemond, C. P. 2004, *ApJ*, **615**, 991
- Kounkel, M., Hartmann, L., Loinard, L., et al. 2017, *ApJ*, **834**, 142
- Kuhn, R. B., Rodriguez, J. E., Collins, K. A., et al. 2016, *MNRAS*, **459**, 4281
- Kurtz, M. J., & Mink, D. J. 1998, *PASP*, **110**, 934
- Latham, D. W. 1992, in Astronomical Society of the Pacific Conference Series, Vol. 32, IAU Colloq. 135: Complementary Approaches to Double and Multiple Star Research, ed. H. A. McAlister & W. I. Hartkopf, 110
- Lomb, N. R. 1976, *Ap&SS*, **39**, 447
- Lynden-Bell, D., & Pringle, J. E. 1974, *MNRAS*, **168**, 603
- Mathieu, R. D., Adams, F. C., Fuller, G. A., et al. 1995, *AJ*, **109**, 2655
- Mathieu, R. D., Adams, F. C., & Latham, D. W. 1991, *AJ*, **101**, 2184
- Murray, C. D., & Correia, A. C. M. 2010, Keplerian Orbits and Dynamics of Exoplanets, ed. S. Seager, 15
- Najita, J., Carr, J. S., & Mathieu, R. D. 2003, *ApJ*, **589**, 931
- Prantzos, N., Aubert, O., & Audouze, J. 1996, *A&A*, **309**, 760
- Rosenfeld, K. A., Andrews, S. M., Hughes, A. M., Wilner, D. J., & Qi, C. 2013, *ApJ*, **774**, 16
- Rosenfeld, K. A., Andrews, S. M., Wilner, D. J., & Stempels, H. C. 2012, *ApJ*, **759**, 119
- Scargle, J. D. 1982, *ApJ*, **263**, 835
- Shappee, B. J., Prieto, J. L., Grupe, D., et al. 2014, *ApJ*, **788**, 48
- Shevchenko, V. S., Grankin, K. N., Ibragimov, M. A., & Melnikov, S. Y. 1992, Information Bulletin on Variable Stars, 3746
- Shevchenko, V. S., Grankin, K. N., Mel'Nikov, S. Y., & Lamzin, S. A. 1998, *Astronomy Letters*, **24**, 528
- Siess, L., Dufour, E., & Forestini, M. 2000, *A&A*, **358**, 593
- Siverd, R. J., Beatty, T. G., Pepper, J., et al. 2012, *ApJ*, **761**, 123

Tognelli, E., Prada Moroni, P. G., & Degl'Innocenti, S.
2011, A&A, 533, A109

Torres, G., Neuhäuser, R., & Guenther, E. W. 2002, AJ,
123, 1701